

# Cavity enhancement of V2 centers in 4H-SiC with a fiber-based Fabry-Pérot microcavity

Jannis Hessenauer <sup>†</sup>, Jonathan Körber <sup>‡</sup>, Misagh Ghezellou <sup>§</sup>, Jawad Ul-Hassan <sup>§</sup>, Georgy V. Astakhov <sup>†</sup>, Wolfgang Knolle <sup>‡</sup>, Jörg Wrachtrup <sup>§</sup>, and David Hunger <sup>†</sup>

<sup>1</sup> Physikalisches Institut, Karlsruhe Institute of Technology (KIT), Wolfgang-Gaede-Str. 1, 76131 Karlsruhe, Germany.

<sup>2</sup> 3rd Institute of Physics, University of Stuttgart, Allmandring 13, 70569 Stuttgart, Germany.

<sup>3</sup> Department of Physics, Chemistry and Biology, Linköping University, 581 83 Linköping, Sweden.

<sup>4</sup> Institute of Ion Beam Physics and Materials Research, Helmholtz-Zentrum Dresden-Rossendorf, 01328 Dresden, Germany.

<sup>5</sup> Leibniz-Institute of Surface Engineering (IOM), Permoserstraße 15, 04318 Leipzig, Germany.

<sup>6</sup> Max Planck Institute for Solid State Research, Heisenbergstraße 1, 70569 Stuttgart, Germany.

<sup>7</sup> Institute for Quantum Materials and Technologies (IQMT), Karlsruhe Institute of Technology (KIT), Herrmann-von-Helmholtz Platz 1, 76344 Eggenstein-Leopoldshafen, Germany.

## Abstract

Silicon vacancy centers in 4H-silicon carbide (SiC) host a long-lived electronic spin and simultaneously possess spin-resolved optical transitions, making them a great candidate for implementing a spin-photon interface. These interfaces are an important building block of quantum networks, which in turn promise to enable secure communication and distributed quantum computing. To achieve this goal, the rate of coherently scattered photons collected from a single emitter needs to be maximized, which can be achieved by interfacing the emitter with an optical cavity. In this work, we integrate V2 centers inside a SiC membrane into a fiber-based Fabry-Pérot microcavity. We find that SiC lends itself well to membrane fabrication, as evidenced by low surface roughness  $\sigma_{\text{RMS}} \approx 400$  pm, high reproducibility, and consequentially a high cavity finesse  $\mathcal{F} \approx 40\,000$ . At cryogenic temperatures, we observe individual emitters coupling to cavity modes. We confirm their single-emitter character by measuring the second-order autocorrelation function and investigate the Purcell factor by measuring the optical lifetime as a function of the cavity-emitter detuning. We find a 13.3-fold enhancement of photons scattered into the zero-phonon line (ZPL), which could be further increased by using optimized mirror coatings, potentially opening the path towards deterministic spin-photon interaction.

## INTRODUCTION

Spin-active quantum emitters in solids are considered a promising platform for quantum technology applications [1, 2]. Diamond, as the main host material for such emitters, has been used for pioneering experiments in the field [3–8]. However, other semiconductor materials such as silicon (Si) [9–11] and SiC [12, 13] have recently gained increasing attention because they offer advantages such as CMOS-fabrication compatibility and wafer-scale material availability [14–17] while still hosting promising quantum emitters, such as silicon-vacancy centers ( $V_{\text{Si}}$ ) [18–20] or divacancy centers (VV) [21–23] in 4H-SiC. The k-site  $V_{\text{Si}}$  (V2)-center in 4H-SiC has already been used for encouraging demonstrations of single-shot readout of the spin state [24, 25] and spin-photon entanglement [26]. However, it shows only low Debye-Waller factors (6–9%) and a moderate quantum efficiency of  $\text{QE}=28.6\%$ , thus raising challenges for useful quantum technology applications with the system [27–30].

Different photonic structures have already been demonstrated to enhance the collected photon rate [31–36]. Yet, to specifically enhance the ZPL transition of the emitters, highly resonant structures that can harness the Purcell ef-

fect must be used. This increases the rate of coherent photons, which are necessary to generate and distribute remote entanglement in quantum networks [2]. Photonic crystal cavities and disk resonators have already been used to enhance  $V_{\text{Si}}$ - and VV-centers in 4H-SiC [37–39]. Compared to these integrated structures, open microcavities such as fiber-based Fabry-Pérot cavities offer the possibility of easy-tunability of the spatial and spectral position of the cavity resonance [40–42]. This enables the in-situ optimization of resonance conditions and the investigation of multiple emitters with a single cavity. With this approach, emitters can be integrated within thin membranes bonded onto the cavity mirror, as already successfully demonstrated for the diamond platform [43–48]. Crucially, this allows one to position emitters farther from surfaces, avoiding spectral diffusion due to charge fluctuations.

In this work, we demonstrate the coupling of V2 centers inside a few-micrometer-thin 4H-SiC membrane to a fiber-based Fabry-Pérot cavity. We produce membranes with an extremely low surface roughness of 350–400 pm RMS and high spatial homogeneity. We study the losses and dispersion of the cavity-membrane system and find excellent agreement with theoretical descriptions and simulations, as well as minimal loss introduced by the membrane. We then analyze the emitter properties and find a reduced lifetime when resonant with the cavity due to the Purcell ef-

\* jannis.hessenauer@kit.edu

† These authors contributed equally to this work.

‡ jonathan.koerber@pi3.uni-stuttgart.de

§ These authors contributed equally to this work.

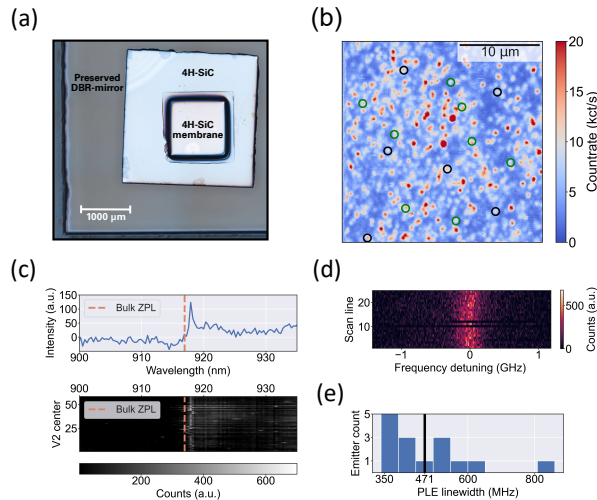


**Figure 1: Fabrication and characterization of the membrane SA.** (a) Light microscope image of the sample after the fabrication. (b) Room temperature confocal fluorescence scan in the membrane region of the sample. Diffraction limited spots that were further investigated by ODMR are marked with a circle. The green circles show spots with a clear ODMR signature from a V2 center. (c) Background corrected emission spectrum of a single spot (upper panel) under off-resonant excitation and integration for 20 seconds at a temperature of 8 K and spectra of 58 investigated V2 centers stacked above each other (lower panel). The orange, dashed line indicates the ZPL position from bulk V2 centers. (d) PLE scans of a single V2 center in the membrane at 8 K. (e) PLE-linewidth distribution of different V2 centers in the membrane. The linewidth is extracted by the average FWHM of Lorentzian fits on 25 single-line PLE scans for each center. The black solid line at 471 MHz depicts the average linewidth of all investigated V2 centers.

fect. Finally, we show that by using the cavity to spectrally select individual emitters, we achieve high single-photon purity and high ZPL count rates.

## RESULTS AND DISCUSSION

### Sample fabrication and characterization

The samples we use for our experiments are made from a commercial, n-type, a-plane 4H-SiC wafer (*Wolfspeed*) with a 10-micron-thick high quality epilayer grown on the top side. In total, we fabricate and investigate two samples, sample A (SA) and sample B (SB). Analogously to previous work [36, 49], we use a series of lapping and chemical-mechanical polishing (CMP) to thin the samples from the wafer side down to a total thickness of  $\sim 40 \mu\text{m}$ . Subsequently, the samples are van der Waals bonded with the epilayer side onto a commercially coated distributed-bragg-reflector (DBR)-mirror (*Laseroptik*), using an oxygen plasma activation (see supplementary materials for details on the bonding procedure). Next, we thin the sam-

ples on the mirror further down to a few  $\mu\text{m}$ -thin membranes using a  $\text{SF}_6$ -based reactive-ion etching (RIE) process. In order to prevent a strong amount of micromasking due to nonvolatile etch by-products from the mirror and to preserve parts of the free mirror throughout the etching, we use a hard mask from SiC wafer material with a square opening on top of SA and only etch it within the opening of the mask, as visible in the microscope image of Figure 1 (a). SB is etched without a hard mask on top. Our etching leaves the surface with a low RMS roughness of  $\sim 400 \text{ pm}$  (see supplementary materials for AFM measurements), which is crucial for high-finesse cavity experiments. To create V2-centers, we use electron irradiation at an energy of 5 MeV and a dose of 5 kGy (see supplementary materials for more information).

To confirm the presence of V2 centers in the fabricated samples, we use a home-built confocal microscope at room temperature (NA=0.9 objective). Figure 1 (b) shows a typical fluorescence map of a central region within the membrane SA under off-resonant excitation at 785 nm. Since the V2 emission spectrum has no characteristic peak at room temperature, we use optically detected magnetic resonance (ODMR) measurements to identify V2 centers together with a preselection based on the polarization of the fluorescence (see [36] for details on the preselection). Out of 14 preselected spots, we find 8 that show a clear ODMR signal from a V2 center (see supplementary information for details on the ODMR measurements).

To characterize the optical properties of the V2 centers in SA, we cool the sample to 8 K in a closed-cycle cryostat (*Montana Instruments*), and use a second home-built confocal microscope (NA=0.75 objective) for cryogenic spectroscopy. Here, we identify V2 centers from their emission spectrum under off-resonant excitation at 730 nm, as shown for an exemplary emitter in the upper panel of Figure 1 (c). Compared to the ZPL of the bulk centers at 917 nm [27, 50], we find that the ZPLs of most emitters in the bonded membrane are shifted by  $\sim 1 \text{ nm}$ , as depicted in the stacked spectra plot of 58 different emitters in the lower panel of Figure 1 (c). We attribute this shift to a homogeneous strain inside the sample arising from the bonding to the DBR-mirror.

Finally, we investigate the linewidths of the optical transitions of membrane-integrated V2 centers by photoluminescence excitation (PLE) scans. As described in earlier work [36], we use acousto-optic modulators (AOMs) to generate a laser beam containing two wavelengths split by 1 GHz. With this beam, we simultaneously scan over both optical transitions of the V2 center at a power of 5 nW before the objective and collect the photons from the phonon sideband (PSB). Figure 1 (d) shows a series of such scans from the same emitter stacked over each other with no visible spectral jumps. To evaluate the linewidth, we fit a Lorentzian to each individual line and extract the mean linewidth from the series. We repeat these measurements for a total of 15 emitters and find a mean PLE linewidth of  $471 \pm 132 \text{ MHz}$  for all emitters, as depicted in Figure 1 (e). To exclude a significant power broadening of the

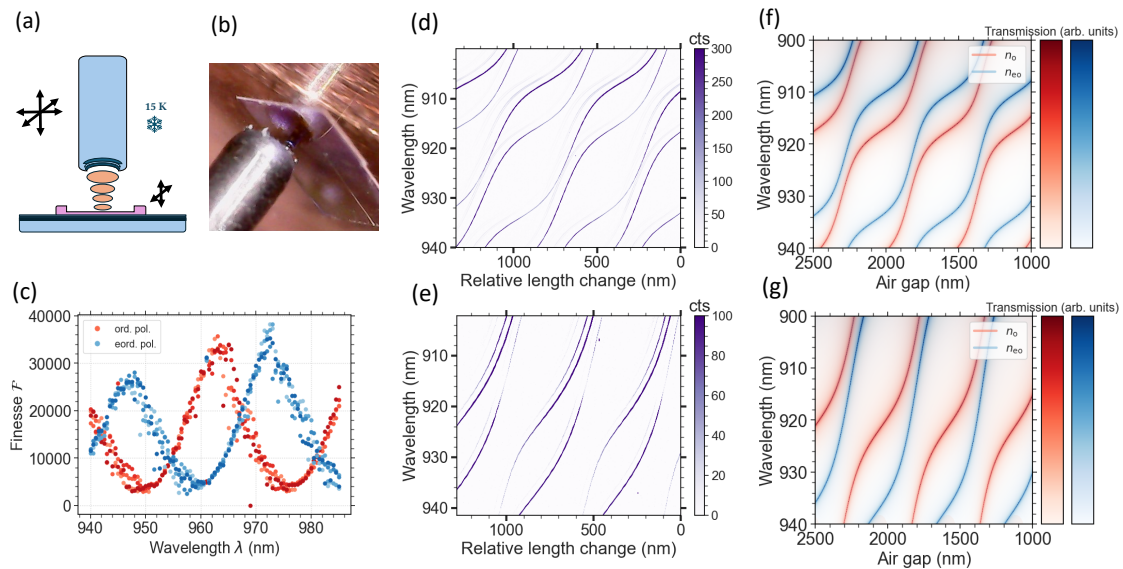


**Figure 2: Characterisation of the membrane cavity system.** (a) Schematic sketch of the fiber-cavity-membrane system. (b) Photograph of the fiber mirror protruding from a metallic needle opposing the membrane bonded onto a planar DBR mirror. (c) Finesse as a function of wavelength for two orthogonal polarisations, corresponding to the ordinary and extraordinary polarization modes of the SiC membrane. The periodic modulation is due to the SiC membrane. (d),(e) Measured cavity dispersion of SA and SB, showcasing the characteristic hybridisation of air-like and dielectric-like modes for membrane cavity systems. Due to the birefringence of SiC, we observe two families of modes. The different membrane thickness changes the periodicity of the mode coupling. (f),(g) Simulated dispersion for SA, SB. The simulation reproduces the measurements. Extracted membrane thicknesses are  $d_{SA} = 6.20 \mu\text{m}$  and  $d_{SB} = 2.85 \mu\text{m}$ .

optical linewidths, we perform excitation power-dependent PLE linewidth measurements on a single emitter and find that there is no significant power broadening at 5 nW excitation power (see supplementary materials). We note that the average PLE linewidth of  $471 \pm 132 \text{ MHz}$  appears to be higher than the linewidth reported from similar samples [36, 49]. Possible explanations for the increased linewidth include non-perfect thermalization of the sample and an increased amount of charge noise, both stemming from the thick, isolating glass substrate of the mirror between the silicon carbide membrane and the copper plate inside the cryostat.

### Cavity characterization

In order to characterize the membrane-mirror system performance, we integrate the sample into a home-built positioning unit, forming a microcavity together with a fiber mirror that is approached closely to the membrane, as sketched in Figure 2 (a) and depicted in Figure 2 (b). The positioning setup is located in a closed-cycle cryostat as reported in earlier work [51]. The fiber mirror can be scanned laterally across the mirror over a range of  $20 \mu\text{m} \times 20 \mu\text{m}$  and the cavity length can be tuned over multiple free spectral ranges. This enables us to spatially search for emitters, optimize the lateral overlap of emitter and cavity mode and then minimize the cavity length by bringing the fiber mirror in contact with the membrane. The contact configuration has the added benefit of drasti-

cally improving the longitudinal stability. This allows us to avoid active stabilization and passively stay on resonance with the ZPL despite a relatively high finesse.

We begin by measuring the finesse at small mirror distance by monitoring the transmission of a narrow linewidth laser through the cavity, while modulating the cavity length over multiple free spectral ranges. The transmission spectrum is fitted with Lorentzians to determine the positions and linewidths of the fundamental modes, allowing us to calculate the finesse. The finesse as a function of the probe wavelength is displayed in Figure 2 (c). It exhibits a strong dependence on the probe wavelength, due to the modulation of the DBR transmission by the membrane. The presence of a membrane in the cavity leads to the formation of a dielectric and air-like set of modes; see [52, 53] and below. We observe a finesse as high as  $\mathcal{F} = 40000$  at a wavelength of  $\lambda = 980 \text{ nm}$ , which is almost twice the value observed for a bare cavity. From simulations with a transfer matrix model, we can extract additional losses due to scattering and absorption in the high-finesse case of approximately  $\mathcal{L}_{\text{air}} \approx 70 \text{ ppm}$ , further evidencing the high sample quality. We measure a finesse of up to  $\mathcal{F} = 10000$  at  $\lambda = 917 \text{ nm}$ , where the zero-phonon line of the V2 center is located.

Next, we measure the dispersion of the cavity-membrane system by coupling a broadband light source to the cavity and observing the resonances in transmission with a spectrometer, while stepwise changing the cavity length (Figure 2 (d) and (e)). The mode hybridization of the

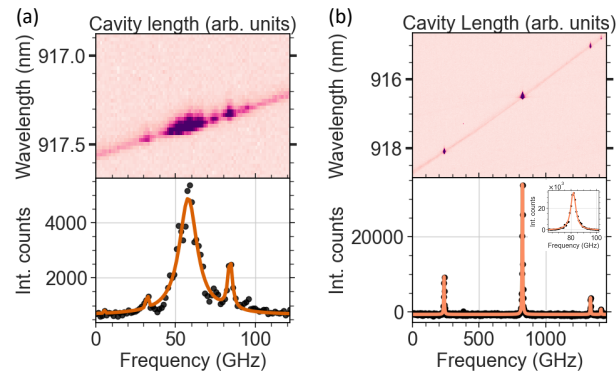


**Figure 3: Coupling of ZPLs to cavity modes** Cavity dispersion measured under off-resonant excitation. A strong increase in emission is observed when the cavity is resonant with the ZPLs. By integrating the individual spectra and calibrating the local dispersion, we can extract a frequency distribution of ZPLs. Notably, the thicker membrane SA (a) shows a denser and more centered distribution of emitters, while SB (b) exhibits sharp peaks with large spacings.

cavity with the membrane manifests itself in a modulation of the cavity dispersion, as previously observed in comparable systems [43, 46, 53–55]. It is further complicated by the strong birefringence of 4H-SiC, which fully determines the polarization modes of the cavity and leads to two families of modes with orthogonal polarization [56]. The two polarization modes are also observed in the finesse measurement (Figure 2 (c)).

Simulated dispersion plots of the cavity membrane system using a transfer matrix model [43] are shown in Figure 2 (f),(g)). The good agreement with the experimental data confirms that our model captures the relevant effects and allows us to extract the membrane thickness of SA to be  $d_{SA} = 6.2\mu\text{m}$  and of SB to be  $d_{SB} = 2.85\mu\text{m}$ , in agreement with the measurements during fabrication using a profilometer.

### Cavity enhanced V2 emission

We continue by measuring the properties of the emitters when coupled to the cavity. We couple an off-resonant diode laser ( $\lambda = 785\text{nm}$ ) to the cavity fiber to excite the emitters via the PSB. The mirror coating is almost transmissive at this wavelength, but still leads to a modulation of the intensity by a factor of  $\approx 3$ , which we account for by measuring the excitation laser power after the cavity. We use filters to block the excitation light and detect the fluorescence in a spectral band of  $\lambda = 900\text{nm} - 1000\text{nm}$ , either using a spectrometer or two single-photon counters arranged in a Hanbury-Brown-Twiss (HBT) configuration.

First, we record spectra under off-resonant excitation while slowly varying the cavity length. Due to a broad background, we observe the cavity dispersion as in Figure 2 (d-e) as well as a strong increase in fluorescence when the cavity is resonant with the ZPL of one or more

V2 centers (Figure 3). Crucially, this is only observed for one polarization branch, because the dipole axis of the V2 center is oriented along the crystallographic c-axis, as is the extraordinary axis of the refractive index ellipsoid (See supplement). This is useful for our application because it guarantees a maximal overlap between the emitter dipole and the cavity polarization, which otherwise would reduce the Purcell factor.

By performing these scans slowly and finely resolved, we notice a substructure around the ZPL of SA (Figure 3 (a)), which we attribute to the inhomogeneous linewidth, originating from the different local electrical environment of multiple emitters. In our sample, multiple emitters are located inside the cavity mode waist, with the depth being randomly distributed. Thus, the lateral overlap and the position in the standing wave field, and therefore the coupling to the cavity mode and the observed peak count rate, vary for the different emitters. Interestingly, emitters in SB are both more sparse and spread over a larger frequency space (Figure 3 (b)). Both facts can possibly be explained by the thinner membrane.

By fitting a linear slope to the local dispersion, we can calibrate the cavity length shift in terms of resonance frequency shift, allowing us to determine the feature linewidth by fitting the calibrated integrated spectrum. The observed linewidth is a convolution of the linewidths of the cavity and the emitter. For sample SB, the brightest peak yields a linewidth of  $\delta\nu = 4.8\text{GHz}$ , while the narrowest linewidth is obtained for the two rightmost peaks with  $\delta\nu = 3.8\text{GHz}$  (lower panel of Figure 3 (b)). We measure the cavity linewidth at this position to be  $\delta\nu_{\text{cav}} = 3.44\text{GHz}$  by slowly (0.1 Hz) scanning a resonant laser over the cavity and recording the frequency with a wavemeter (see Supplement). This indicates a contribution from the emitter linewidth for the most dominant peak, which could be caused by insufficient thermalization of the mirror in the cavity stage. The temperature we measure at the mirror holder is 16 K. The linewidth of V2 centers is known to significantly increase above 20 K [27]. However, the sample is isolated from the copper mirror holder by the mirror substrate. To alleviate this, we add a copper link connecting the mirror holder to the sample, but a temperature gradient might nevertheless still persist.

Even though multiple emitters are located inside the cavity mode volume, we can make use of their inhomogeneous spectral distribution together with the spectral selectivity of the cavity to select individual emitters. In the thinner membrane SB, we observe peaks that are well isolated and are spread over a wide spectral range (918–923 nm). We set the cavity resonant with the brightest peak and measure the second-order autocorrelation  $g^{(2)}(\tau)$  under pulsed off-resonant excitation (SuperK-Fianium, repetition rate 23.4 MHz,  $\lambda = 780\text{nm} - 790\text{nm}$ ,  $P = 230\mu\text{W}$ ). The measurement and a fit are displayed in Figure 4 (c). We observe a strong antibunching dip at  $\tau = 0\text{ns}$  with  $g^{(2)}(0) = 0.024 \pm 0.024$ , indicating a high single-photon purity. This underlines the ability of the cavity to spectrally

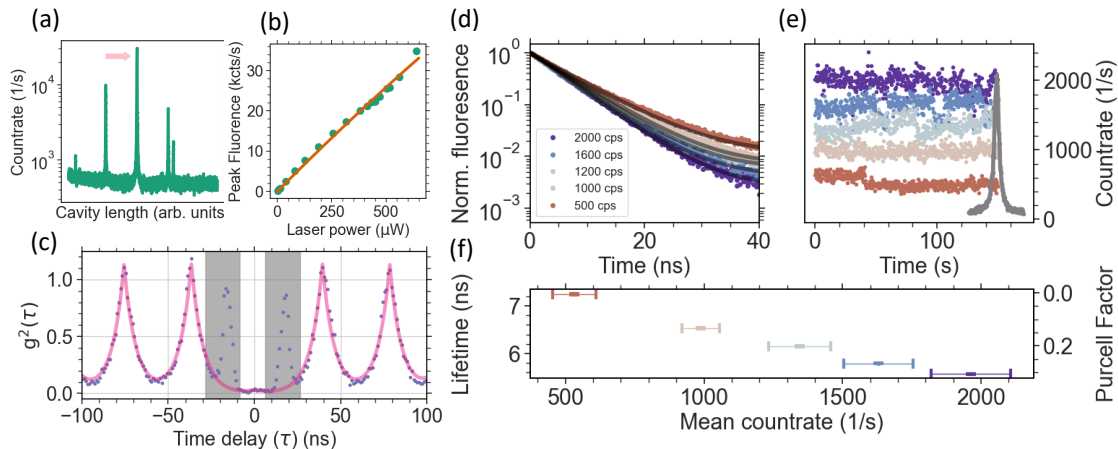


**Figure 4: Characterization of the emitter fluorescence in the cavity.** (a) Detected count rate under off-resonant, pulsed excitation as a function of cavity detuning. At least four distinct peaks belonging to different ZPLs are visible. The brightest peak shows a ZPL count rate of 30 kcps. Note the close similarity to the measurement in Figure 3 (b), when accounting for the different y-axis scaling. (b) Excitation power dependence of the ZPL count rate under pulsed excitation. Laser power was measured behind the cavity. No clear saturation behaviour observed. (c) Pulsed autocorrelation measurement with the cavity resonant with the peak marked in (a), showcasing a high single-photon purity of  $g^{(2)}(0) = 0.024 \pm 0.024$  without background correction. Coincidence counts in the gray area arise from recombination photons in the counting APDs and are excluded from the fit (see Supplement for details). (d) Detuning dependent optical lifetime measurements of the resonance marked in (a). The detuning is reflected by the average count rate during the measurement. Solid lines show monoexponential fits with a constant offset to account for background counts. The count rate traces are plotted together with a sweep over the resonance in (e). The lifetime reduces as the cavity becomes resonant with the ZPL, consistent with Purcell enhancement. The effective Purcell factors calculated from  $C = \frac{\tau_0}{\tau} - 1$  are plotted in (f).

select single emitters even under non-selective excitation, potentially enabling spectral multiplexing.

In order to quantify the achieved Purcell enhancement, we conduct lifetime measurements using the same pulsed laser source as above by recording the start-stop histograms between the laser emission and the detected photons. We vary the cavity emitter detuning and observe a lifetime-shortening as the cavity becomes resonant with the ZPL (see Figure 4 (d-f)). The shortest lifetime observed when the cavity and the emitter line coincide is  $\tau_{\min} = 5.6$  ns. We take the longest lifetime observed for large detunings as the free space lifetime  $\tau = 7.3$  ns, in good agreement with the values reported in the literature, e.g.  $\tau = 7.08$  ns in [57]. The lifetime shortening allows us to determine the effective Purcell factor defined as  $C_{\text{eff}} = \frac{\tau_0}{\tau_{\text{cav}}} - 1 = 0.30 \pm 0.01$ . The observed change in the lifetime is small because only the photons emitted into the narrow ZPL experience a significant Purcell enhancement, while all other decay channels remain unperturbed. Taking into account the fraction of coherently emitted photons via the Debye-Waller factor of  $\text{DWF} = 8\%$  [27] and accounting for the quantum efficiency of  $\text{QE} = 28.6\%$  [30], this corresponds to an ideal Purcell factor  $C_0 = C_{\text{eff}} / (\text{DWF} \cdot \text{QE}) = 13.3$ . The ideal Purcell factor quantifies how many ZPL photons are additionally emitted into the cavity mode compared to free-space emission into  $4\pi$ .

## Discussion

For calculating the expected Purcell factor, we use the quality factor  $Q = 7.4 \times 10^4$  extracted from the dispersion measurement (Fig 3 (c) inset), which is sensitive to both the linewidth of the cavity and the emitter. The mode volume  $12.0 \lambda_{V2}^3$  is calculated by numerically integrating the field distribution obtained by the 1D-simulation, yielding the effective cavity length  $L_{\text{eff}} = \frac{\int |n(z)E(z)|^2 dz}{\max(n(z)E(z))}$ . The mode volume is then given by  $V = \frac{\pi w_0^2 L_{\text{eff}}}{4}$ , where the mode waist  $w_0 = 1.66 \mu\text{m}$  in the membrane is calculated as previously reported in [43, 52] by matching a Gaussian beam in the air gap to one in the membrane. This results in an expected Purcell factor of  $C_0 = 25.7$ . By using the quality factor obtained in the dispersion measurement, we automatically account for additional broadening of the emitters in the calculation, which could be caused by insufficient thermalization. Yet, the calculated value is almost twice as high as the observed Purcell enhancement. We believe that this difference can be explained by a non-perfect overlap of the defect with the cavity mode field, both transversally and longitudinally. Further, our calculations of the ideal Purcell factor depend on literature values for the Debye-Waller factor and the quantum efficiency. While these properties have been studied carefully in the past, it is unclear how they are affected by a thin membrane, in particular because of applied stress.

However, even a relatively small lifetime reduction due to the small QE and DWF leads to a large increase of ZPL photons by a factor of  $C_0$ , which is confirmed by the observed ZPL count rates of up to 30 kcts/s (Figure 4 (a)). We note that we use conventional silicon-based single photon counters, which feature a smaller detection efficiency (detection efficiency  $\approx 30\%$ ) than the commonly used superconducting nanowire detectors (detection efficiency  $\approx 90\%$ ). Furthermore, due to the limited available pulsed laser power and inefficient excitation due to the large cavity mode waist, we are unable to saturate the emitter. This is evident from both the saturation measurement depicted in Figure 4 (b) and the rather unpronounced bunching in  $g^{(2)}(\tau)$  displayed in Figure 4 (c). We estimate that by driving the emitter in saturation, we could increase the count rate by at least a factor of four. Therefore, we predict that we can achieve more than an order of magnitude higher count rates by using a more potent laser source and state of the art single photon detectors, without any changes to the cavity-membrane system.

## Summary and Outlook

In conclusion, we have demonstrated Purcell enhancement of single V2 centers in a few-micron-thick 4H-SiC membrane by integrating the membrane in a fiber-based Fabry-Pérot cavity. The suitability of SiC for this approach is evident by the reproducible fabrication process, excellent surface roughness, and experimentally observed high finesse. We find a lifetime reduction of  $C_{\text{eff}} = 0.30$ , which corresponds to a 13.3-fold enhancement of the coherent zero-phonon line. The spectral selectivity of the cavity allows us to achieve a high single-photon purity even though multiple defects are spatially located inside the cavity field. We detect up to 30 kcts/s ZPL photons from a single emitter, which could be increased by more than an order of magnitude by updating the experimental setup with state of the art technology.

In future work, the Purcell factor could be increased by utilizing an optimized mirror coating with the stopband centered around the ZPL resonance. Operating an experiment with a finesse of  $\mathcal{F} = 40\,000$ , as measured in the center of the stopband for our mirror, requires extremely low cavity fluctuations, which, however, have been demonstrated for the setup used in this work using active stabilization. This would enable ten times higher effective Purcell factors of up to  $C_{\text{eff}} = 3$ . For spectrally narrow emitters close to the lifetime limit, as already demonstrated for V2 centers in even thinner membranes [49], this corresponds to a cooperativity  $C > 1$ , enabling spin-based reflection schemes which can be harnessed to generate remote entanglement [58]. Another important step forward is to demonstrate control of the spin state, either by integrating an RF line into the setup or by coherently driving the optical transitions.

## DATA AVAILABILITY

The data to reproduce the figures in the main text and the figures in the Supporting Information are available at **Link to data repository will be provided at later stage.**

## CODE AVAILABILITY

The measurement and evaluation codes used for this study are available from the corresponding author upon reasonable request.

## COMPETING INTERESTS

The authors declare no competing interests.

## ACKNOWLEDGEMENTS

We acknowledge fruitful discussions and experimental help from F. Kaiser, J. Heiler, K. Köster, S. Müller, M. Pallmann, R. Wörnle, T. Steidl, D. Liu, P. Kuna and V. Vorobyov.

J.H. and D.H. acknowledge funding from the Karlsruhe School of Optics and Photonics (KSOP). J.H., D.H. and J.W. acknowledge funding by the German Federal Ministry of Education and Research (BMBF) within the project QR.X (Contract No. 16KISQ004).

J.W. further acknowledges funding by the German research foundation (DFG, Grant agreement No. GRK2642), the Baden-Württemberg Stiftung via the project SPOC (Grant agreement No. QT-6), as well as the BMBF via the project InQuRe (Grant agreement No. 16KIS1639K) and the Clusters4Future QSENS project QVOL. J.W. and J.U.H. acknowledge the European Union (EU) within the Horizon Europe project SPINUS (Grant agreement No. 101135699) and the QuantERA project InQuRe (Grant agreements No. 731473 and 101017733).

J.U.H. further acknowledges funding by the Swedish Research Council under VR Grant No. 2020-05444.

G.A. gratefully acknowledges support from the Ion Beam Center (IBC) at HZDR for ion implantation.

## References

1. Atatüre, M., Englund, D., Vamivakas, N., Lee, S. Y. & Wrachtrup, J. Material platforms for spin-based photonic quantum technologies. *Nat. Rev. Mater.* **3**, 38–51 (2018).
2. Awschalom, D. D., Hanson, R., Wrachtrup, J. & Zhou, B. B. Quantum technologies with optically interfaced solid-state spins. *Nat. Photonics* **12**, 516–527 (2018).
3. Gaebel, T. *et al.* Room-temperature coherent coupling of single spins in diamond. *Nat. Phys* **2**, 408–413 (2006).
4. Balasubramanian, G. *et al.* Nanoscale imaging magnetometry with diamond spins under ambient conditions. *Nature* **455**, 648–651 (2008).
5. Neumann, P. *et al.* Single-shot readout of a single nuclear spin. *Science* **329**, 542–544 (2010).

6. Hensen, B. *et al.* Loophole-free Bell inequality violation using electron spins separated by 1.3 kilometres. *Nature* **526**, 682–686 (2015).
7. Bradley, C. E. *et al.* A Ten-Qubit Solid-State Spin Register with Quantum Memory up to One Minute. *Phys. Rev. X* **9**, 031045 (2019).
8. Pompili, M. *et al.* Realization of a multinode quantum network of remote solid-state qubits. *Science* **372**, 259–264 (2021).
9. Durand, A. *et al.* Broad Diversity of Near-Infrared Single-Photon Emitters in Silicon. *Phys. Rev. Lett.* **126**, 083602 (2021).
10. Higginbottom, D. B. *et al.* Optical observation of single spins in silicon. *Nature* **607**, 266–270 (2022).
11. Hollenbach, M. *et al.* Wafer-scale nanofabrication of telecom single-photon emitters in silicon. *Nat. Commun.* **13**, 1–7 (2022).
12. Castelletto, S. *et al.* Silicon carbide color centers for quantum applications. *JPhys Photonics* **2**, 022001 (2020).
13. Castelletto, S. *et al.* Silicon Carbide Photonics Bridging Quantum Technology. *ACS Photonics* **9**, 1434–1457 (2022).
14. Ryu, S. H., Kornegay, K. T., Cooper, J. A. & Melloch, M. R. Digital CMOS IC's in 6H-SiC operating on a 5-V power supply. *IEEE Trans. Electron Devices* **45**, 45–53 (1998).
15. Hassan, J., Bergman, J. P., Henry, A. & Janzén, E. On-axis homoepitaxial growth on Si-face 4H-SiC substrates. *J. Cryst. Growth* **310**, 4424–4429 (2008).
16. Liu, G., Tuttle, B. R. & Dhar, S. Silicon carbide: A unique platform for metal-oxide-semiconductor physics. *Appl. Phys. Rev.* **2**, 021307 (2015).
17. Yang, T. *et al.* Demonstration of 4H-SiC CMOS digital IC gates based on the mainstream 6-inch wafer processing technique. *J. Semicond.* **43**, 082801–1 (2022).
18. Kraus, H. *et al.* Room-temperature quantum microwave emitters based on spin defects in silicon carbide. *Nat. Phys* **10**, 157–162 (2014).
19. Widmann, M. *et al.* Coherent control of single spins in silicon carbide at room temperature. *Nat. Mater.* **14**, 164–168 (2015).
20. Nagy, R. *et al.* High-fidelity spin and optical control of single silicon-vacancy centres in silicon carbide. *Nat. Commun.* **10**, 1–8 (2019).
21. Son, N. T. *et al.* Divacancy in 4H-SiC. *Phys. Rev. Lett.* **96**, 055501 (2006).
22. Christle, D. J. *et al.* Isolated spin qubits in SiC with a high-fidelity infrared spin-to-photon interface. *Phys. Rev. X* **7**, 021046 (2017).
23. Li, Q. *et al.* Room-temperature coherent manipulation of single-spin qubits in silicon carbide with a high readout contrast. *Natl. Sci. Rev.* **9** (2022).
24. Lai, X.-Y. *et al.* Single-Shot Readout of a Nuclear Spin in Silicon Carbide. *Phys. Rev. Lett.* **132**, 180803 (2024).
25. Hesselmeier, E. *et al.* High fidelity optical readout of a nuclear spin qubit in Silicon Carbide. *Phys. Rev. Lett.* **132**, 180804 (2024).
26. Fang, R.-Z. *et al.* Experimental Generation of Spin-Photon Entanglement in Silicon Carbide. *Phys. Rev. Lett.* **132**, 160801 (2024).
27. Udvarhelyi, P. *et al.* Vibronic States and Their Effect on the Temperature and Strain Dependence of Silicon-Vacancy Qubits in 4H-SiC. *Phys. Rev. Appl.* **13**, 054017 (2020).
28. Son, N. T. *et al.* Developing silicon carbide for quantum spintronics. *Appl. Phys. Lett.* **116**, 12 (2020).
29. Shang, Z. *et al.* Local vibrational modes of Si vacancy spin qubits in SiC. *Phys. Rev. B* **101**, 144109 (2020).
30. Liu, D. *et al.* The silicon vacancy centers in SiC: determination of intrinsic spin dynamics for integrated quantum photonics. *npj quantum inf.* **10**, 1–9 (2024).
31. Radulaski, M. *et al.* Scalable Quantum Photonics with Single Color Centers in Silicon Carbide. *Nano Lett.* **17**, 1782–1786 (2017).
32. Sardi, F. *et al.* Scalable production of solid-immersion lenses for quantum emitters in silicon carbide. *Appl. Phys. Lett.* **117**, 22105 (2020).
33. Bekker, C. *et al.* Scalable fabrication of hemispherical solid immersion lenses in silicon carbide through grayscale hard-mask lithography. *Appl. Phys. Lett.* **122**, 173507 (2023).
34. Zhou, J. Y. *et al.* Plasmonic-Enhanced Bright Single Spin Defects in Silicon Carbide Membranes. *Nano Lett.* **23**, 4334–4343 (2023).
35. Krumrein, M. *et al.* Precise Characterization of a Waveguide Fiber Interface in Silicon Carbide. *ACS Photonics* **11**, 2160–2170 (2024).
36. Körber, J. *et al.* Fluorescence Enhancement of Single V2 Centers in a 4H-SiC Cavity Antenna. *Nano Lett.* **13**, 53 (2024).
37. Crook, A. L. *et al.* Purcell enhancement of a single silicon carbide color center with coherent spin control. *Nano Lett.* **20**, 3427–3434 (2020).
38. Lukin, D. M., Guidry, M. A. & Vučković, J. Integrated Quantum Photonics with Silicon Carbide: Challenges and Prospects. *PRX Quantum* **1**, 020102 (2020).
39. Lukin, D. M. *et al.* Two-Emitter Multimode Cavity Quantum Electrodynamics in Thin-Film Silicon Carbide Photonics. *Phys. Rev. X* **13**, 011005 (2023).
40. Hunger, D. *et al.* A fiber Fabry–Perot cavity with high finesse. *New J. Phys.* **12**, 065038 (2010).
41. Toninelli, C. *et al.* A scanning microcavity for in situ control of single-molecule emission. *Appl. Phys. Lett.* **97**, 021107 (2010).

42. Mader, M., Reichel, J., Hänsch, T. W. & Hunger, D. A scanning cavity microscope. *Nat. Commun.* **6**, 1–7 (2015).
43. Janitz, E. *et al.* Fabry-Perot microcavity for diamond-based photonics. *Phys. Rev. A* **92**, 43844 (2015).
44. Riedel, D. *et al.* Deterministic enhancement of coherent photon generation from a nitrogen-vacancy center in ultrapure diamond. *Phys. Rev. X* **7**, 031040 (2017).
45. Heupel, J. *et al.* Fabrication and Characterization of Single-Crystal Diamond Membranes for Quantum Photonics with Tunable Microcavities. *Micromachines* **11**, 1080 (2020).
46. Salz, M. *et al.* Cryogenic platform for coupling color centers in diamond membranes to a fiber-based microcavity. *Appl. Phys. B: Lasers and Optics* **126**, 1–13 (2020).
47. Ruf, M., Weaver, M. J., Van Dam, S. B. & Hanson, R. Resonant Excitation and Purcell Enhancement of Coherent Nitrogen-Vacancy Centers Coupled to a Fabry-Perot Microcavity. *Phys. Rev. Applied* **15**, 024049 (2021).
48. Pallmann, M. *et al.* Cavity-Mediated Collective Emission from Few Emitters in a Diamond Membrane. *Phys. Rev. X* **14**, 041055 (2024).
49. Heiler, J. *et al.* Spectral stability of V2 centres in sub-micron 4H-SiC membranes. *npj quantum mater.* **9** (2024).
50. Wagner, M. *et al.* Electronic structure of the neutral silicon vacancy in 4H and 6H SiC. *Phys. Rev. B* **62**, 16555 (2000).
51. Pallmann, M. *et al.* A highly stable and fully tunable open microcavity platform at cryogenic temperatures. *APL Photonics* **8** (2023).
52. Van Dam, S. B., Ruf, M. & Hanson, R. Optimal design of diamond-air microcavities for quantum networks using an analytical approach. *New. J. Phys.* **20**, 115004 (2018).
53. Körber, J. *et al.* Scanning Cavity Microscopy of a Single-Crystal Diamond Membrane. *Phys. Rev. Applied* **19**, 64057 (2023).
54. Høy Jensen, R. *et al.* Cavity-Enhanced Photon Emission from a Single Germanium-Vacancy Center in a Diamond Membrane. *Phys. Rev. Appl.* **13**, 64016 (2020).
55. Maisch, J. *et al.* Investigation of Purcell enhancement of quantum dots emitting in the telecom O-band with an open fiber-cavity. *Phys. Rev. B* **110**, 165301 (2024).
56. Xing, P. *et al.* CMOS-Compatible PECVD Silicon Carbide Platform for Linear and Nonlinear Optics. *ACS Photonics* **6**, 1162–1167 (2019).
57. Babin, C. *et al.* Fabrication and nanophotonic waveguide integration of silicon carbide colour centres with preserved spin-optical coherence. *Nat. Mater.* **21**, 67–73 (2022).
58. Nemoto, K. *et al.* Photonic architecture for scalable quantum information processing in diamond. *Phys. Rev. X* **4**, 031022 (2014).



## Supplementary materials to: Cavity enhancement of V2 centers in 4H-SiC with a fiber-based Fabry-Pérot microcavity

Jannis Hessenauer,<sup>1,\*</sup> Jonathan Körber,<sup>2,\*</sup> Misagh Ghezellou,<sup>3</sup> Jawad Ul-Hassan,<sup>3</sup>  
Georgy V. Astakhov,<sup>4</sup> Wolfgang Knolle,<sup>5</sup> Jörg Wrachtrup,<sup>2,6</sup> and David Hunger<sup>1,7</sup>

<sup>1</sup>Physikalisches Institut, Karlsruhe Institute of Technology (KIT),  
Wolfgang-Gaede-Str. 1, 76131 Karlsruhe, Germany.

<sup>2</sup>3rd Institute of Physics, University of Stuttgart, Pfaffenwaldring 57, 70569 Stuttgart, Germany.

<sup>3</sup>Department of Physics, Chemistry and Biology, Linköping University, 581 83 Linköping, Sweden.

<sup>4</sup>Institute of Ion Beam Physics and Materials Research,

Helmholtz-Zentrum Dresden-Rossendorf, 01328 Dresden, Germany.

<sup>5</sup>Leibniz-Institute of Surface Engineering (IOM), Permoserstraße 15, 04318 Leipzig, Germany.

<sup>6</sup>Max Planck Institute for Solid State Research, Heisenbergstraße 1, 70569 Stuttgart, Germany.

<sup>7</sup>Institute for Quantum Materials and Technologies (IQMT), Karlsruhe Institute of Technology (KIT),  
Herrmann-von-Helmholtz Platz 1, 76344 Eggenstein-Leopoldshafen, Germany.

(Dated: January 9, 2025)

### S1. DETAILS ON THE SAMPLE FABRICATION

#### A. Main samples of the study

For both samples of our the experiments in the main manuscript (SA and SB), a commercial n-type a-plane 4H-SiC wafer (*Wolfspeed*) is used. After a one-sided commercial chemical-mechanical polishing (*NovaSiC*), n-type epilayers with a thickness of  $\sim 10 \mu\text{m}$  are grown along the a-axis on the polished side by chemical vapor deposition (CVD). For SA the isotope concentration is not controlled, leading to a natural abundance of isotopes in the epilayer. SB is taken from a different batch of epilayer growth, where the isotopes are controlled to 0.5%  $^{13}\text{C}$  and 0.5%  $^{29}\text{Si}$  in the CVD of the epilayer. We note that we do not expect significant differences from the varying isotope concentrations for our experiments at this stage, and we simply chose the two different epilayers on the basis of the availability of our samples. As stated in the main manuscript, we use a hard mask for the RIE process of SA, mainly to prevent micromasking during the etching, yielding only a small membrane part of the sample. For SB we

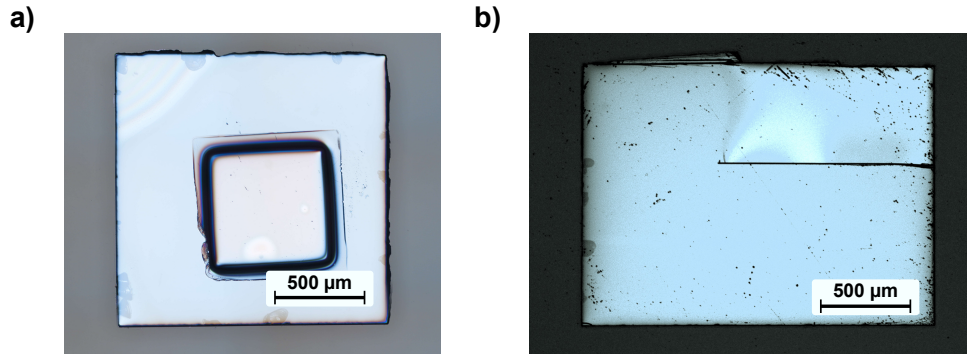


**Figure S1:** Light microscope images of the samples after the final etching. Microscope image of the finalized samples SA (a) and SB (b). The use of a hard mask yields a membrane only within a square sub-region of SA, while SB is fully thinned down. In comparison of both etched parts (membrane part of (a) and full region of (b)) one can see a clear difference in the density of etching pits (black dots).

\* These authors contributed equally to this work

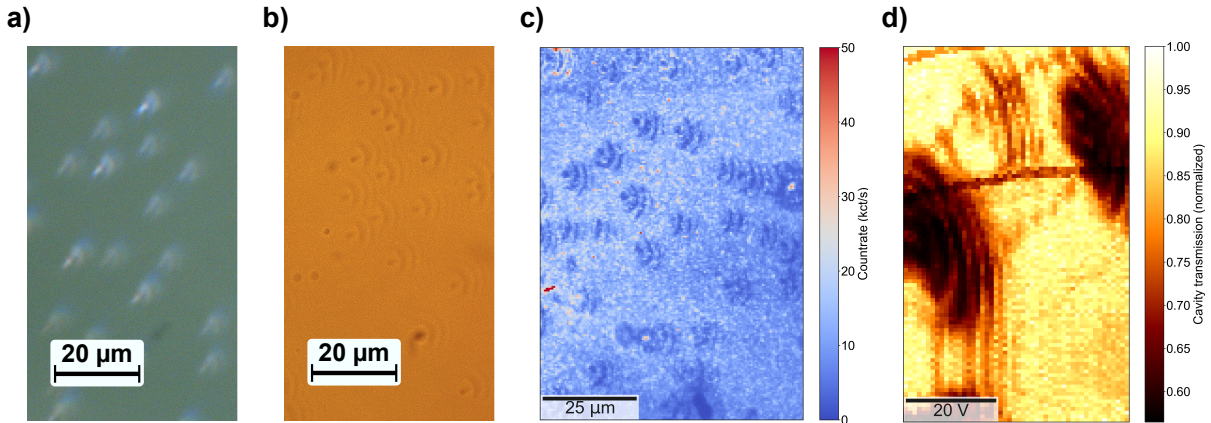


**Figure S2:** Optically visible defects in the SiC epilayer of SB. Light microscope images of SB after bonding (a) and after the final etching (b). For image (a) the dark-field mode of the microscope is used, while image (b) is taken with the light-field mode. Both images show a high number of spots with a similar pattern. (c) Fluorescence map of SB taken in a room-temperature confocal microscope taken with  $850 \mu\text{W}$  of excitation power (785 nm). The defects are visible in a decrease of fluorescence brightness. (d) Cavity transmission scan of SB. The scale bar shows the voltage steps of the piezo, leading to the lateral cavity displacement.

decide to etch without the hard mask to achieve a larger region at the desired thickness. As can be seen in the microscope images of both samples after fabrication in figure S1, the absence of a hard mask during etching leads to a higher density of etching marks for SB. However, the density of pits remains small enough compared to the lateral dimension of the cavity mode in our experiments, so that we are able to reach high-finesse values of  $\sim 40\,000$  for both samples. As stated in the main text, we use electron irradiation for both samples to create V2-centers in the fabricated membranes. However, for SA we tried to create V2-centers using proton-implantation through a 400 nm-thick PMMA mask with circular openings (diameters of 200–400 nm) in the first place. We used protons with an energy of 27 keV and a dose of  $4 \times 10^{11} \text{ cm}^{-2}$  for implantation. After we have not found V2 emission in the fiber cavity, we decided to additionally perform electron irradiation with this sample. In contrast, SB is electron irradiated already before fabrication. The electron irradiation is performed with an energy of 5 MeV and a dose of 5 kGy for both samples. The dose was determined by means of a 5 mm-thick graphite calorimeter for the nominal energy of 10 MeV. The nominal energy was reduced with a 10 mm-thick aluminum plate to be about 5 MeV onto the samples. The electron fluence can be calculated from the dose using the known average stopping power. For this, we use a conversion factor of  $3.6 \text{ kGy} \hat{=} 1 \times 10^{13} \text{ cm}^{-2}$ . Thus, 5 kGy correspond to a nominal fluence of  $\sim 1.4 \times 10^{13} \text{ cm}^{-2}$ . The use of the 10 mm-thick aluminum plate leads to a loss of some lower-energy components of the electron beam and therefore to a slight reduction in the total electron fluence, which, however, is less than 10%.

### B. Optically visible defects within sample B

During the fabrication of SB, we became aware of optically visible defects inside the epilayer of the SiC sample. As shown in Figs. S2 (a) and (b), these defects were already visible during the course of fabrication. After the fabrication and color center creation, we investigate the fluorescence of the sample in a room temperature confocal microscope and find those defects again, see Figure S2 (c). As expected, those defects lead to increased scattering of light in the fiber cavity experiments and thus are visible in a decreased cavity finesse and transmission, as depicted in figure figure S2 (d). We suspect that those defects originate from the epilayer growth. During the epitaxial growth process, a silicon-rich environment initially leads to the formation of Si droplets on the surface of the substrate at the start of the growth. However, as the growth processes, these droplets recrystallize into perfect SiC, leaving behind characteristic surface morphological features, as observed in the optical images of sample SB. Such defects are purely surface morphological in nature and do not represent any form of extended defects. Compared to the lateral mode extension of our fiber cavity, the density of the surface morphological features is small enough to find spots where the cavity can be operated without experiencing additional extinction.

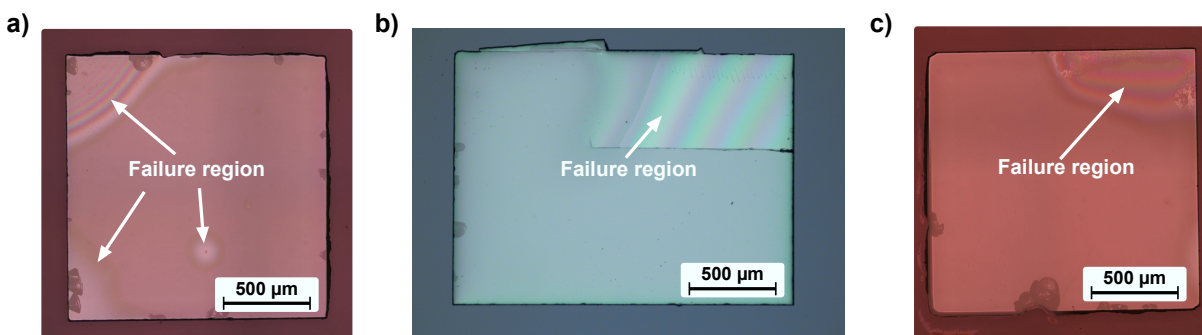


**Figure S3:** Light microscope images of the SiC samples after the Van der Waals bonding. Light microscope image of SA (a), SB (b), and a third sample that was bonded with the same procedure but used for a different study (c). All images were taken after the bond anneal. White arrows point towards regions where the contact bond failed which is visible through interference fringes, arising from the small airgap between the SiC and the mirror substrate.

### C. Van der Waals bonding

In order to integrate the membrane samples into the fiber cavity, we bond them onto mirror substrates using Van der Waals forces, as described in the main manuscript. Once established, this results in a very strong bond between the SiC and the mirror enabling us to further process the samples, i.e. cleaning with organic solvents, dry etching and performing all the measurements in the cavity. To create the Van der Waals bond, we use the following recipe for our samples: First, the SiC samples are thoroughly cleaned by wiping cleanroom tissues dipped into acetone with strong pressure over the sample. This is repeated using isopropanol instead of acetone. The whole wiping is repeated until almost no remaining particles are visible on the surface under a light field microscope at high (50x) magnification. At next, the SiC and the mirror surface are activated using an oxygen plasma [1]. For half of the samples we use an activation within our RIE-ICP machine (*PlasmaPro80, Oxford Instruments*) with an RF and ICP power of 100 W, a pressure of 50 mTorr, an oxygen gas flow of 30 sccm and a time of 2 minutes. For the other half of our samples we use a softer treatment within a plasma cleaner (*Pico plasma cleaner, diener*) at an ICP power of 100 W a pressure of 3 mTorr, an oxygen gas flow of 30 sccm and a time of 5 minutes, i.e. entirely without a directed plasma as it is used in the RIE-ICP. After the activation, we place each sample on top of a mirror substrate and apply manual pressure using the thumb and a small glass slide on top of the sample. Now, the sample should be already pre-bonded and not move anymore when applying pressure with tweezers from the side. After a successful pre-bond, we place the sample on a hot plate at maximum temperature of 200 °C for several hours in order to strengthen the bond (bond anneal) [1]. The results of the samples SA, SB and a further sample from a different study are shown in figure S3. Apart from a few smaller regions, where the bond failed (visible by interference fringes stemming from the small airgap underneath), the samples are successfully Van der Waals bonded. With this recipe, we find a success rate of 2/3 and after repeating the process for the failed samples we are able to achieve a strong bond for all of our samples. Since we don't see differences in the success rate between both plasma activation steps, we decide to use the softer activation by the plasma cleaner for future experiments.

### D. AFM roughness after the fabrication

As we have seen in previous work [2], the surface RMS-roughness does not significantly change during the RIE process compared to the roughness after our polishing process. This is shown for SA with AFM measurements in figure S4. Throughout the deep etching, the scratches that are left on the surface after the polishing (see figure S4 (a)) eventually vanish, leaving an even more homogeneous surface after the etching (see figure S4 (b) and (c)), which is beneficial for our cavity experiments.

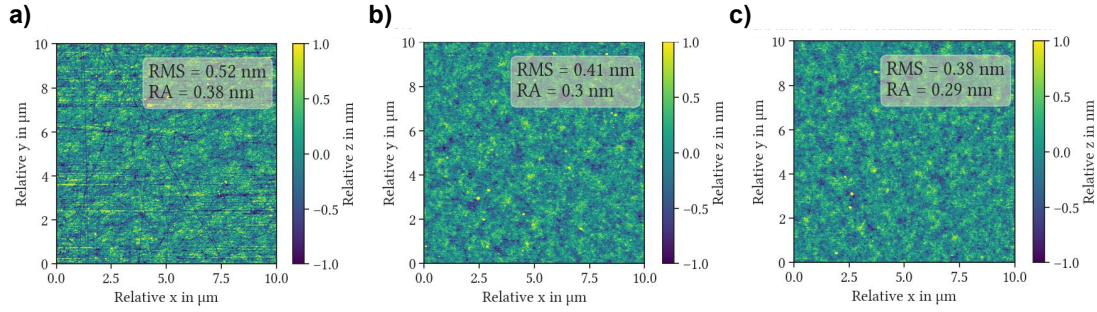


**Figure S4:** AFM measurements for surface roughness characterization of SA. AFM measurements of the surface of SA after the polishing (a) and for two different regions within the etched membrane (b) + (c). The RMS and RA deviation of the mean height of the surface are shown on the upper right.

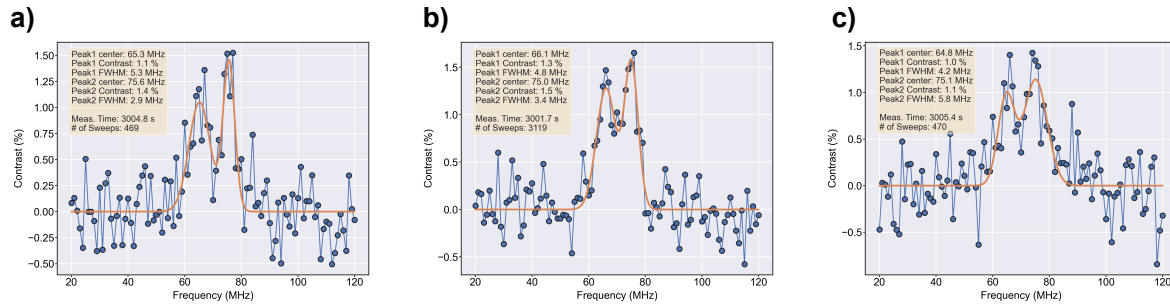


**Figure S5:** ODMR signal from several fluorescent spots of SA at room temperature. ODMR measurement at  $600\ \mu\text{W}$  of optical excitation power and 19–20 dbm of microwave input power at three different spots on SA (a)-(c). Blue dots show the measurement results and the blue line is a guide to the eye. Solid, orange lines show a double-Lorentzian fit on the measured data.

## S2. ODMR MEASUREMENTS FOR V2 IDENTIFICATION AT ROOM TEMPERATURE

As discussed in the main manuscript, we perform ODMR measurements in our room temperature confocal setup on SA to identify V2 centers among all fluorescent spots. To perform the measurements, we use a  $50\ \mu\text{m}$ -thick copper wire spanned across the sample with a distance below  $100\ \mu\text{m}$  to the investigated emitters. We send a microwave signal from a signal generator (*SMIQ03, Rohde & Schwarz*) after amplification (*LZY-22+, Mini Circuit*) to 19–20 dbm through the wire while optically exciting with  $600\ \mu\text{W}$  at  $785\ \text{nm}$ . When sweeping the microwave frequency, we expect a positive signal in the fluorescence at  $70\ \text{MHz}$  for V2 centers [3]. All spots with a clear ODMR contrast of  $\sim 1\%$  or larger are counted as V2 centers in our statistics, as shown for three representative spots in figure S5. We note that in our case the single ODMR peak is split into two peaks. This has been already seen in previous work with the setup [4] and most likely is a result of a magnetization of the objective.

## S3. PLE MEASUREMENTS AT DIFFERENT EXCITATION POWER AND TEMPERATURE

To ensure that the PLE linewidths of our measurements on several emitters are not broadened due to a high excitation power or the temperature in the cryostation, we measure the PLE linewidth on a single V2 center as a function of the excitation power and the set cryostation temperature. To extract the PLE linewidth, we fit a Lorentzian on 25 single line scans for each excitation power (temperature) and extract the average and the standard deviation of all single lines. As shown in Figure S6 (a), the average linewidth starts to plateau at an excitation power of  $5\ \text{nW}$ . Thus, we decide to measure PLE for all further spots with  $5\ \text{nW}$  of excitation power. Similarly, the PLE linewidth plateaus at a set temperature below  $10\ \text{K}$  of the cryostation, indicating that the measurements discussed in the

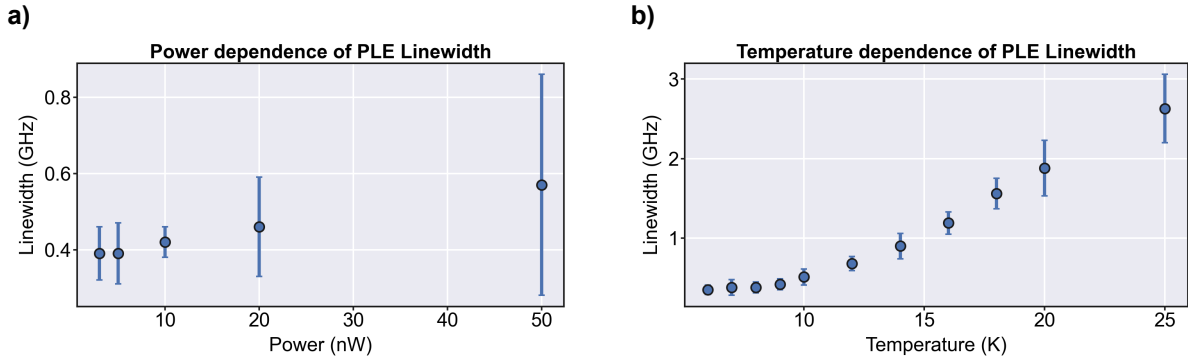


**Figure S6:** Excitation power and temperature dependence of PLE linewidth. Mean PLE linewidth for different excitation power at a set temperature of 8 K (a) and different set temperature of the cryostat at a fixed excitation power of 5 nW (b). The linewidths are the average of 25 single line PLE scans for each point. The errorbars indicate the standard deviation of each average linewidth.

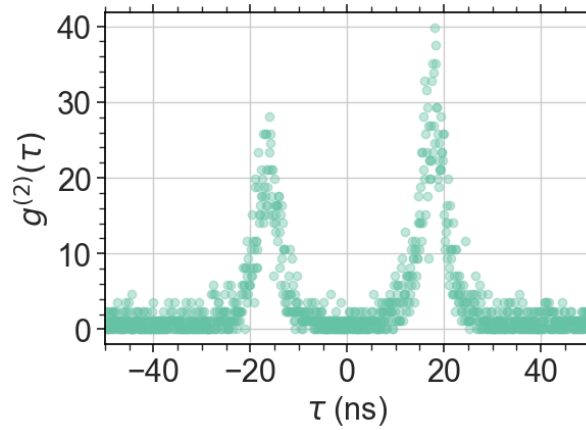


**Figure S7:** Characteristic background in the  $g^{(2)}$  measurement. Data was taken with the cavity far detuned from any resonance under cw illumination, such that the overall countrate is given by the background.

main manuscript at a set temperature of 8 K are not limited by temperature, as well. We note that the rather large standard deviation of the mean PLE linewidths for higher excitation powers is a result of a higher number of ionization events within the 25 single line scans of our measurements. Since we do not exclude those lines from the average, the standard deviation becomes larger, while we are still able to extract the maximum excitation power without a broadening of the optical line.

#### S4. RECOMBINATION BACKGROUND IN THE $G^{(2)}$ MEASUREMENT

When measuring second order autocorrelation functions, we always observe two characteristic peaks at time delay of  $\pm 17$  ns, as depicted in Figure S7. We attribute this to radiative recombination and relaxation processes in the silicon chips of the single photon counting modules, that are seen by the other detector, as previously observed [5]. The time delay corresponds to an optical path length of  $d = 5.2$  m, which is twice the distance between the cavity and the detectors. We observe these features regardless of the analysed light (Emitter and background fluorescence, narrow laser light or broadband light sources transmitted through the cavity, scattered flash-light radiation when illuminating only the detection path). Only the height of the features in the autocorrelation varies depending on the total countrate.

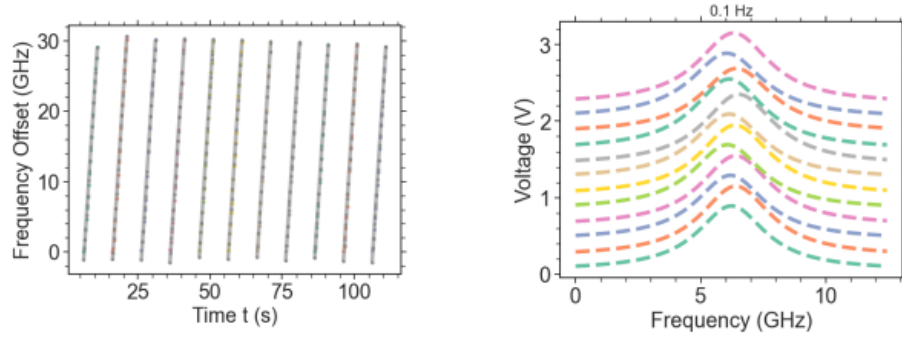


**Figure S8:** Measurement of the cavity linewidth. (a) To calibrate the cavity linewidth, wavemeter readings are recorded and fit with a linear slope. (b) 12 succinct fits to scans of the cavity line with 0.1 Hz, offset by 0.2 V each. The average linewidth is  $\Delta\nu \approx 3.44$  GHz.

Notably, the peaks disappear when we illuminate the detectors while blocking the optical path from/to the cavity. We therefore attribute these peaks to backscattering of such recombination photons from the cavity. It is astonishing that the effect is so clearly visible, because only a small fraction of the photons emitted by this process should be guided in this specific optical mode.

Unfortunately, we can not spectrally filter this background, since it overlaps with the ZPL emission. Another approach that has been used previously was to utilize a combination of polarisers and polarizing beam splitter to isolate the detectors from each other [6]. In fact, the polarizing beam-splitter used in the HBT here should already serve this role. But even with added polarization filters, we were unable to remove the artifacts completely. Therefore, we simply choose to exclude them from our fits. However, this precludes a more detailed analysis of the  $g^2$  function that is useful to depend the rates governing the system, especially if done in a power dependent manner [7].

## S5. CAVITY LINEWIDTH AND STABILITY

We measure the cavity linewidth under the same conditions and at the same membrane position where we record the Purcell and  $g^{(2)}(\tau)$  measurements depicted in Figure 4 of the main text. Therefore, we scan a laser tuned close to the emitter linewidth over the stationary cavity resonance and record the resonance. We calibrate the scan speed by fitting a linear slope to the recorded wavelength over time trace recorded with a wavemeter. We then fit the calibrated cavity line with a Lorentzian, yielding linewidths of  $\Delta\nu \approx 3.44$  GHz for a scan speed of 6 GHz/s and  $\Delta\nu \approx 4.05$  GHz for a scan speed of 0.6 GHz/s. The difference is likely due to small drifts on long timescales. Exemplary linewidth measurements are depicted in Figure S8.

We also measure the cavity stability under cryogenic conditions by recording a fast fourier transform (FFT) of the cavity transmission while positioning the laser on the side of fringe of the cavity line. We can then calibrate the FFT amplitude in length fluctuations by the cavity finesse  $\mathcal{F}$  [8]. This results in  $\sigma_{\text{RMS}} \approx 45$  pm under normal operation and  $\sigma_{\text{RMS}} \approx 16$  pm when the fiber mirror is brought into contact with the membrane-mirror system (see Figure S9).

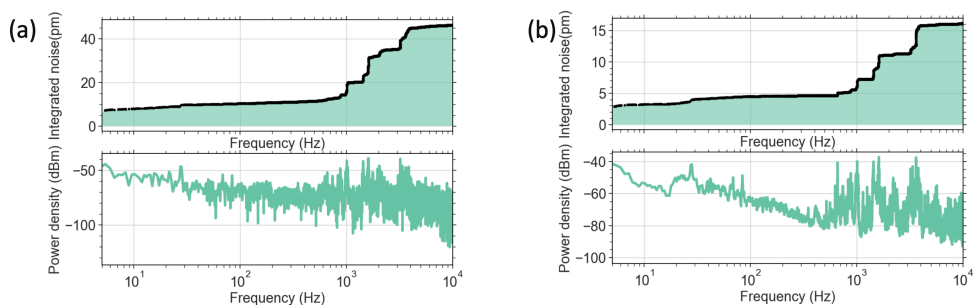


**Figure S9:** Cumulative rms noise of the cavity and corresponding noise spectrum measured (a) for a free fiber mirror and (b) when the fiber mirror is brought in contact with the membrane-mirror system.

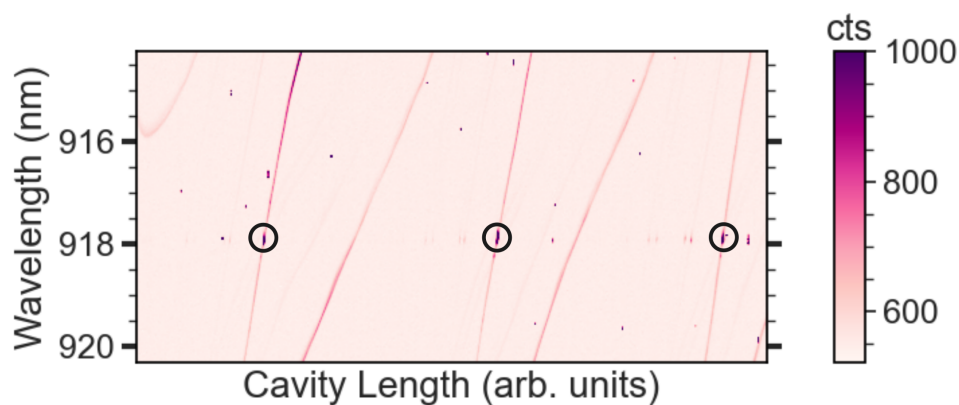


**Figure S10:** Cavity dispersion scan under off-resonant illumination. Only one set of modes couples to ZPLs (marked by black circles).

## S6. BIREFRINGENCE

As mentioned in the main text, only one set of modes, corresponding to the extraordinary refractive index of the membrane, couples to the ZPLs of V2 centers. This is evident in a dispersion measurement under off resonant excitation at  $\lambda = 785$  nm, as depicted in Figure S10. The extraordinary and ordinary refractive index modes are distinguished by their different slope. It is evident that only one set of modes couples to the V2 center ZPL.

- 
- [1] Q. Kang, C. Wang, F. Niu, S. Zhou, J. Xu, and Y. Tian, Single-crystalline SiC integrated onto Si-based substrates via plasma-activated direct bonding, *Ceram. Int.* **46**, 22718 (2020).
- [2] J. Heiler, J. Körber, E. Hesselmeier, P. Kuna, R. Stöhr, P. Fuchs, M. Ghezellou, J. Ul-Hassan, W. Knolle, C. Becher, F. Kaiser, and J. Wrachtrup, Spectral stability of V2 centres in sub-micron 4H-SiC membranes, *npj quantum mater.* **9**, 10.1038/s41535-024-00644-4 (2024).
- [3] H. Kraus, V. A. Soltamov, D. Riedel, S. Vãth, F. Fuchs, A. Sperlich, P. G. Baranov, V. Dyakonov, and G. V. Astakhov, Room-temperature quantum microwave emitters based on spin defects in silicon carbide, *Nat. Phys.* **10**, 157 (2014).
- [4] J. Körber, J. Heiler, P. Fuchs, P. Flad, E. Hesselmeier, P. Kuna, J. Ul-Hassan, W. Knolle, C. Becher, F. Kaiser, and J. Wrachtrup, Fluorescence Enhancement of Single V2 Centers in a 4H-SiC Cavity Antenna, *Nano Lett.* **13**, 53 (2024).
- [5] C. Kurtsiefer, P. Zarda, S. Mayer, and H. Weinfurter, The breakdown flash of silicon avalanche photodiodes-back door for eavesdropper attacks, *J. Mod. Opt.* **48**, 2039 (2001).
- [6] M. Radulaski, M. Widmann, M. Niethammer, J. L. Zhang, S.-Y. Lee, T. Rendler, K. G. Lagoudakis, N. T. Son, E. Janzén, T. Ohshima, J. Wrachtrup, and J. Vučković, Scalable Quantum Photonics with Single Color Centers in Silicon Carbide, *Nano Lett.* **17**, 1782 (2017).
- [7] M. Pallmann, K. Köster, Y. Zhang, J. Heupel, T. Eichhorn, C. Popov, K. Mølmer, and D. Hunger, Cavity-Mediated Collective Emission from Few Emitters in a Diamond Membrane, *Phys. Rev. X* **14**, 041055 (2024).
- [8] M. Pallmann, T. Eichhorn, J. Benedikter, B. Casabone, T. Hümmer, and D. Hunger, A highly stable and fully tunable open microcavity platform at cryogenic temperatures, *APL Photonics* **8**, 10.1063/5.0139003 (2023).